Geomechanics and Engineering, *Vol. 23, No. 6 (2020) 561-573*
DOI: https://doi.org/10.12989/gae.2020.23.6.561

Thermal volume change of saturated clays: A fully coupled thermo-hydro-mechanical finite element implementation

Hao Wang[1,2] and Xiaohui Qi*[3]

[1]Department of Civil Engineering, Tsinghua University, Beijing 100084, China
[2]Beijing Key Laboratory of Urban Underground Space Engineering, School of Civil and Resource Engineering,
University of Science and Technology Beijing, Beijing 100083, China
[3]School of Civil and Environmental Engineering, Nanyang Technological University, Singapore 639798, Singapore

(Received August 20, 2020, Revised November 21, 2020, Accepted December 16, 2020)

Abstract. The creep and consolidation behaviors of clays subjected to thermal cycles are of fundamental importance in the application of energy geostructures. This study aims to numerically investigate the physical mechanisms for the temperature-triggered volume change of saturated clays. A recently developed thermodynamic framework is used to derive the thermo-mechanical constitutive model for clays. Based on the model, a fully coupled thermo-hydro-mechanical (THM) finite element (FE) code is developed. Comparison with experimental observations shows that the proposed FE code can well reproduce the irreversible thermal contraction of normally consolidated and lightly overconsolidated clays, as well as the thermal expansion of heavily overconsolidated clays under drained heating. Simulations reveal that excess pore pressure may accumulate in clay samples under triaxial drained conditions due to low permeability and high heating rate, resulting in thermally induced primary consolidation. Results show that four major mechanisms contribute to the thermal volume change of clays: (i) the principle of thermal expansion, (ii) the decrease of effective stress due to the accumulation of excess pore pressure, (iii) the thermal creep, and (iv) the thermally induced primary consolidation. The former two mechanisms mainly contribute to the thermal expansion of heavily overconsolidated clays, whereas the latter two contribute to the noticeable thermal contraction of normally consolidated and lightly overconsolidated clays. Consideration of the four physical mechanisms is important for the settlement prediction of energy geostructures, especially in soft soils.

Keywords: thermal consolidation; thermal creep; saturated clay; thermodynamic constitutive model; thermo-hydro-mechanical; finite element

1. Introduction

The thermally induced volume change of clays has been studied in the context of applications including nuclear waste disposal, oil and gas exploration, CO_2 storage, and, recently, energy foundations (e.g., Baldi *et al.* 1988, Hueckel and Pellegrini 1992, Brandl 2006, Stewart and McCartney 2014, Song *et al.* 2020). Under drained conditions, a monotonic temperature increase or a heating-cooling cycle may induce irreversible volumetric contraction for normally consolidated and lightly overconsolidated clays, whereas the same loading condition may result in volumetric expansion for heavily overconsolidated clays. The laboratory-scale phenomena have been reported in both oedometric (Towhata *et al.* 1993, Abuel-Naga *et al.* 2006, 2007b, Vega and McCartney 2015) and triaxial tests (Baldi *et al.* 1988, Sultan *et al.* 2002, Cekerevac and Laloui 2004, Di Donna and Laloui 2015a, Bai and Shi 2017). The accumulation of the irreversible thermal contraction with thermal cycles is essential for the prediction of the long-term settlement of energy geostructures, for example, energy piles in soft clays (Li *et al.* 2019). Therefore, the physical mechanisms behind the thermal contraction need to be quantitatively investigated.

To understand the thermal volume change of clays, a number of thermo-mechanical constitutive models have been proposed based on either the critical state framework or the thermodynamic theory. A review of the literature shows that some models based on the critical state framework can well reproduce the thermal volume change of clays of different overconsolidation ratios (OCR) (e.g., Hueckel and Borsetto 1990, Cui *et al.* 2000, Sultan *et al.* 2002, Abuel-Naga *et al.* 2007b, Laloui and François 2009, Di Donna and Laloui 2015a, Zhou and Ng 2018, Zhu *et al.* 2019). The irreversible thermal contraction under constant confining stresses and complete drainage, also known as the thermal creep (Vega and McCartney 2015, Li *et al.* 2018), is explained by the shrinkage of yield surface with increasing temperature. In the meantime, extensive laboratory experiments have proved that the thermal creep is physically related to the micro-scale interactions between clay particles and the adsorbed water (e.g., Plum and Esrig 1969, Morinl and Silva 1984, Towhata *et al.* 1993, Villar and Lloret 2004, Osipov 2012). In this sense, models extended from the thermodynamic theory (e.g., Zhang and Cheng 2016, 2017, Zymnis *et al.* 2018a) possess advantages over the Cam-Clay-family models in that the concept of

---

*Corresponding author, Ph.D.
E-mail: qixiaohui@ntu.edu.sg

http://www.techno-press.org/?journal=gae&subpage=7

ISSN: 2005-307X (Print), 2092-6219 (Online)

adsorbed water is implemented for the physical explanation of the thermal creep. According to the thermodynamic models, at elevated temperature, part of the adsorbed water, which plays an important role in the transmission of interparticle contact forces, converts into free water. The free water can be easily squeezed out of the contact region, resulting in the loss of mechanical balance and the irreversible reorganization of clay particles (Zhang and Cheng 2017).

In practice, however, the thermal volume change of clays cannot be explained completely based on the constitutive level simulations. Considering the low permeability of soft clays, the complete drainage condition is sometimes difficult to be achieved for heating tests with drainage boundaries, even at laboratory scale. Excess pore pressure can be generated within the sample due to the difference in the thermal expansion coefficient of water and soil particles. For example, Vega and McCartney (2015) conducted a series of thermal cyclic tests of Bonny clay in a temperature-regulated oedometer. Only the upper boundary of the samples was set as the drainage boundary, and the samples were heated from 18°C to 91°C with a heating rate of 1.54°C/h. A maximum excess pore pressure of 0.7% of the axial stress was measured at the bottom of the normally consolidated sample during heating. Zhang and Kurimoto (2016) reproduced the triaxial drained heating test conducted by Cekerevac and Laloui (2004) using a finite element-finite difference analysis. They observed an excess pore pressure of 7% of the isotropic confining stress at the center of the normally consolidated Kaolin sample. As a result, apart from the mechanism of thermal creep, the thermally induced excess pore pressure and the corresponding primary consolidation can also contribute to the overall thermal volume change of the clay sample. The complete drainage condition for low permeable saturated soils requires a very low heating rate, which usually cannot be achieved in field applications. Furthermore, the heat sources in these tests were located outside the samples, so that the heat transfer within the samples should be a transient problem (Cekerevac and Laloui 2004, Abuel-Naga *et al.* 2006). Therefore, in these tests and in field scale applications, the uneven distribution of temperature and excess pore pressure within the soils should be carefully analyzed, which can only be achieved through numerical tools such as finite element (FE) analysis (Di Donna and Laloui 2015b, Cui *et al.* 2020, Tamizdoust and Ghasemi-Fare 2020).

Despite the progress reported in the literature, few numerical studies have investigated the physical mechanisms for the thermal volume change of saturated clays. In this study, a fully coupled thermo-hydro-mechanical (THM) finite element formulation is developed for this purpose. The extended granular solid hydrodynamic (GSH) model (Zhang and Cheng 2016, 2017, Zymnis *et al.* 2015, 2018a) is taken as the constitutive model, which has been proved to be able to well capture the thermal behaviors of clays on the constitutive level. The model follows the thermodynamic approach and takes the mechanism related to the adsorbed water as the major thermoplastic dissipation mechanism. After a brief description of the model, the new FE governing equations in the mechanical field, the hydraulic field and the thermal field are introduced, respectively. The dynamic viscosity and the thermal expansion coefficient of the pore fluid are considered to be temperature dependent, so that the excess pore pressure distribution can be reasonably predicted. Finally, FE analyses of the triaxial heating tests by Cekerevac and Laloui (2004) and the one-dimensional heating tests by Abuel-Naga *et al.* (2006) are performed. In both cases, the thermally induced creep and consolidation are discussed in detail. The study aims to gain insight into the specific physical mechanisms that contribute to the magnitude and OCR dependence of the thermal volume change of clays.

2. Brief description of the extended GSH model

The extended GSH model adopts the dry density ρ_d, the elastic strain tensor ε_{ij}^e, the temperature T, and the granular temperature T_g as independent state variables. The concept of granular temperature has been extensively used in research fields such as grain flow and rapid flow of nearly elastic particles since the 1980s. Only recently, it has been adopted by the GSH theory (Jiang and Liu 2007) to describe the granular solids in quasi-static states. T_g is not a real temperature and has a dimension different from that of temperature. It is a state variable that quantitatively describes the local intensity of kinetic energy dissipation, which is the sum of microscopic phenomena such as sliding, rolling and collision of particles. Therefore, T_g determines the irrecoverable strain and the irrecoverable strain rate. Under isothermal conditions, T_g is generated by the random particle motions caused by the external stimulations. Under nonisothermal conditions, T_g can also be generated by the mass exchange from adsorbed water to free water, as will be discussed later.

The model assumes that the clay is fully saturated and is composed of solid and liquid phases. The liquid phase is further separated into free water and adsorbed water for the consideration of thermoplasticity (thermal creep). It is also assumed that the bound water is completely absorbed on the surface of the solid particles.

Based on Hertz contact (Johnson 1987) and granular elasticity, the elastic potential function of the extended GSH model considering the thermo-elastic coupling is expressed as (Zhang and Cheng 2016)

$$\omega_e = B(\varepsilon_v^e + c)^{1.5}\left[0.4(\varepsilon_v^e)^2 + \xi(\varepsilon_s^e)^2\right] + \int K_e \beta_T (T - T_0)\, d\varepsilon_v^e \quad (1)$$

where $B = B_0 exp(B_1 \rho_d)$ is a density-dependent variable with the same dimensions as the stress, B_0, B_1, c, and ξ are elastic parameters, ε_v^e and ε_s^e are the elastic volumetric strain and the second elastic strain invariant, respectively, $K_e = 0.4B(\varepsilon_v^e + c)^{0.5}(3.5\varepsilon_v^e + 2c)$ is the secant bulk modulus of the soil skeleton, T_0 is the reference temperature, β_T is the volumetric thermal expansion coefficient of the soil skeleton, defined by $\beta_T = \beta_s + (\phi_b/\phi_s)\beta_b$, β_s and β_b are the volumetric thermal expansion coefficients of the solid phase and adsorbed water phase, respectively, and ϕ_s and ϕ_b are the volume fractions of the solid phase and adsorbed water phase, respectively. The definitions and units of the parameters are illustrated in Table 1. The model takes the compression positive sign convention. By the commonly

Table 1 List of parameters as the input of the THM-coupled finite element analysis

Category	Parameter	Unit	Definition and function
Isothermal hyperelasticity	B_0	[Pa]	Elastic parameter, controlling the location of VCL
	B_1	[m^3/kg]	Elastic parameter, controlling the slope of VCL
	c	[--]	Elastic parameter related to cohesion
	ξ	[--]	Elastic parameter, affecting dilation and state boundary surface
Isothermal plasticity	m_1	[--]	Migration coefficient, controlling the rate of elastic relaxation
	m_2	[min^2]	Migration coefficient, controlling the rate of granular temperature increase induced by the change of shear strain
	m_3	[--]	Migration coefficient, controlling the rate of granular temperature increase induced by the change of volumetric strain
	m_4	[kg/m^3/min]	Migration coefficient, controlling the conversion rate from granular entropy to real entropy
Thermoelastic coupling	β_s	[°C^{-1}]	Volumetric thermal expansion coefficient of solid phase
	ϕ_{b0}	[--]	Initial volume fraction of adsorbed water
	ρ_{s0}	[kg/m^3]	Initial intrinsic density of solid phase
Thermoplastic coupling	α_{bf}	[°C^{-1}]	The mass change from unit mass of adsorbed water to free water in response to unit temperature rise
	k_g	[°C^{-1}]	Thermoplastic parameter, affecting the magnitude of thermally induced dissipation
	m_6	[kg/m^3/Pa]	Thermoplastic parameter, affecting the magnitude of thermally induced dissipation
Intrinsic permeability	κ_0	[m^2]	Parameter relating to intrinsic permeability
	b_k	[--]	Parameter relating to intrinsic permeability
Energy conservation equation	c_s	[J/kg/°C]	Heat capacity of solid phase
	λ	[W/m/K]	Thermal conductivity of the system

used hyperelastic relationship, the effective stress can be expressed as

$$\sigma_{ij}' = \frac{\partial \omega_e}{\partial \varepsilon_{ij}^e} = B(\varepsilon_v^e + c)^{0.5}\left[1.4(\varepsilon_v^e)^2 + 0.8c\varepsilon_v^e + 1.5\xi(\varepsilon_s^e)^2\right]\delta_{ij} + 2B\xi(\varepsilon_v^e + c)^{1.5} + K_e\beta_T(T - T_0)\delta_{ij} \quad (2)$$

Similar to the elasto-plastic models, the total strain rate herein is decomposed into the sum of the elastic strain rate and the irrecoverable (plastic) strain rate $\dot{Y}_{ij}$. According to the relaxation time concept (Jiang and Liu 2009), $\dot{Y}_{ij}$ is further assumed to be a function of the elastic strain and the granular temperature. The total strain rate is thereby expressed as

$$\dot{\varepsilon}_{ij} = \dot{\varepsilon}_{ij}^e + \dot{Y}_{ij} = \dot{\varepsilon}_{ij}^e + [m_1(T_g)^{0.5}\varepsilon_v^e\delta_{ij} + (T_g)^{0.5}e_{ij}^e] \quad (3)$$

where m_1 is a migration coefficient, e_{ij}^e is the deviatoric elastic strain, and e_{ij} is the Kronecker delta.

To solve the irrecoverable strain rate, the evolution of granular temperature is quantitatively expressed as (Zhang and Cheng 2016)

$$\begin{aligned} &\dot{T}_g = \frac{m_2 m_4}{\rho_d}\left[m_3(\dot{\varepsilon}_v)^2 + (\dot{\varepsilon}_s)^2\right] + \frac{m_5\sigma'_{kk}\,\alpha_b\phi_b}{3\phi_s\rho_d}\dot{T} - \frac{m_4}{\rho_d}T_g \\ &\text{with } m_5(T) = \begin{cases} m_6\exp\left[k_g(T - T_0)\right] & T > 0 \\ 0 & T \le 0 \end{cases}, \text{ and } \phi_b(T) = \phi_{b0}\exp\left[-\alpha_b(T - T_0)\right] \end{aligned} \quad (4)$$

where m_2–m_6 are migration coefficients, α_{bf} represents the mass change from the unit mass of adsorbed water to free water in response to a unit temperature rise, k_g is a material constant, and ϕ_{b0} is the initial volume fraction of adsorbed water.

The first term on the right of the equation represents the isothermal increase of T_g, which leads to isothermal plasticity (Wang and Cheng 2017). The second term indicates the thermally induced production rate of T_g. It is the key thermo-plastic mechanism in the model and the main reason for the thermal creep. The mechanism states that a thinner adsorbed water layer will lead to the irreversible particle rearrangement and the thermal contraction of clays. The mechanism has been proved by experimental observations (e.g., Plum and Esrig 1969, Morinl and Silva 1984, Villar and Lloret 2004, Osipov 2012). The third term is the dissipation rate of T_g towards real temperature.

Lastly, the dry density is calculated following the mass conservation equation

$$\dot{\rho}_d = \rho_d\dot{\varepsilon}_v \quad (5)$$

Altogether, 13 parameters are involved in the model: 4 isothermal hyperelastic parameters, 4 isothermal plastic parameters, 2 thermoelastic parameters and 3 thermoplastic parameters. The parameters and their definitions are listed in Table 1. The calibration process of the parameters can be found in Zhang and Cheng (2016, 2017) and Zymnis *et al.* (2015, 2018a).

According to the calibration tests by Xu *et al.* (2009) and Hiebl and Maksymiw (1991), the thermal expansion coefficients of free water and adsorbed water can be expressed as

$$\begin{aligned} \beta_l(T) &= -5.38\times10^{-5} + 1.53\times10^{-5}\times T - 1.34\times10^{-7}\times T^2 \\ &\quad + 6.48\times10^{-10}\times T^3 + 1.96\times10^{-24}\times T^4 - 5.31\times10^{-26}\times T^5 \\ \beta_b(T) &= [11941.50 - 0.27\times T + 0.07\times T^2 - 2.24\times10^{-4}\times T^3 \\ &\quad - 11591.52\times(\frac{T + 273.15}{228} - 1)^{-0.025}]\times10^{-4} \end{aligned} \quad (6)$$

Theoretically, the model can account for the isothermal mechanical creep of clays during the drained heating. However, because of the lack of calibration tests, the simulations hereinafter are considered to be rate independent.

3. Axisymmetric FE formulation of coupled THM process

3.1 Mechanical field formulation

The present formulation takes (r, z, θ) as the radial, axial, and circumferential coordinates, respectively, of the global axisymmetric coordinate system. Displacement, pore pressure, and temperature are adopted as nodal degrees of freedom. An instantaneous temperature equilibrium is assumed between local clay particles and pore liquids, and no phase change is assumed for water under elevated temperature.

For the mechanical field, the incremental form of the equilibrium equation is expressed as

$$\begin{cases} \nabla_r \cdot \{\dot{\sigma}\} - \{\dot{g}\}[\rho_d + \rho_l(1-\dfrac{\rho_d}{\rho_s})] = 0 \\ \nabla_r = \begin{bmatrix} \partial/\partial r + 1/r & -1/r & 0 & \partial/\partial z \\ 0 & 0 & \partial/\partial z & \partial/\partial r + 1/r \end{bmatrix} \end{cases} \tag{7}$$

where $\{\sigma\} = [\sigma_r, \sigma_\theta, \sigma_z, \tau_{rz}]^{\mathrm{T}}$ is the total stress vector, $\{g\} = [g_r, g_z]^{\mathrm{T}}$ is the gravity vector, and ρ_s and ρ_l are the intrinsic densities of particles and liquids, respectively. The Terzaghi formulation of effective stress states $\{\sigma\} = \{\sigma'\} + p\{m\}$, where $\{\sigma'\} = [\sigma_r', \sigma_\theta', \sigma_z', \tau_{rz}']^{\mathrm{T}}$ is the effective stress vector, p is the pore pressure, and $\{m\} = [1, 1, 1, 0]^{\mathrm{T}}$. Then, substitute Eqs. (2), (3) and (5) into Eq. (7), and by computing the total differentiation of the effective stress with respect to the elastic strain, the temperature and the total strain yields

$$\nabla_r \cdot \{([D_\varepsilon]+[D_\rho])\{\dot{\varepsilon}\} - [D_\varepsilon]\{\dot{Y}\} + [D_T]\dot{T} + \dot{p}\{m\}\} - \{\dot{g}\}[\rho_d + \rho_l(1-\frac{\rho_d}{\rho_s})] = 0 \tag{8}$$

where $\{\varepsilon^e\} = [\varepsilon_r{}^e, \varepsilon_\theta{}^e, \varepsilon_z{}^e, \gamma_{rz}{}^e]^{\mathrm{T}}$, $\{\varepsilon\} = [\varepsilon_r, \varepsilon_\theta, \varepsilon_z, \gamma_{rz}]^{\mathrm{T}}$, $\gamma_{rz}{}^e = 2\varepsilon_{rz}{}^e$, and $\gamma_{rz} = 2\varepsilon_{rz}$. The matrices $[D_\varepsilon]$, $[D_T]$, $[D_\rho]$ and $\{\dot{Y}\}$ are defined in the Appendix. The granular temperature in $\{\dot{Y}\}$ is solved by Eq. (4).

In this study, the standard Galerkin method is used for the spatial discretization of the governing equations. Define the shape function of displacement, pore pressure, and temperature as N, N_p, and N_T, respectively, and their corresponding nodal vectors as $\{a\}$, $\{p\}$, and $\{T\}$. Also, define the strain matrix as $\{\varepsilon\} = -B\{a\}$. Then, the axisymmetric mechanical governing equation considering the stress vector $\{s\} = [s_r, s_z]^{\mathrm{T}}$ on the stress boundary S_σ is given by

$$[K]\{\dot{a}\} - [K_p]\{\dot{p}\} - [K_T]\{\dot{T}\} = \{F\} \tag{9}$$

where $[K]$, $[K_p]$, and $[K_T]$ represent the mechanical term, the HM-coupled term, and the TM-coupled term, respectively, on the mechanical response. The detailed expressions of the matrices are given in the Appendix.

3.2 Hydraulic field formulation

The saturated soil is assumed to be composed of the solid phase and the liquid phase. Define $\{v_s\}$, $\{v_l\}$, and $\{v_t\} = \{v_l\}-\{v_s\}$ as the velocity vector of the solid phase, the velocity vector of the liquid phase, and the relative velocity vector of liquids to solids, respectively. Darcy's law is then expressed as

$$\{v\} = \phi_l\{v_t\} = -\frac{\kappa}{\mu}(\nabla p - \rho_l\{g\})$$
$$\text{with } \kappa(\phi_l) = \kappa_0 \exp\left(\frac{b_k}{1-\phi_l}\right), \ \mu(T) = 1.984\times10^{-6}\exp(\frac{1825.85}{T+273.15}), \tag{10}$$
$$\text{and } \rho_l(T) = \rho_{l0}\left[1-\beta_l(T-T_0)\right]$$

where $\{v\}$ denotes the vector of seepage velocity, κ_0 and b_k denote material constants for the intrinsic permeability κ, ϕ_l denotes the volume fraction of the liquid phase, μ denotes the dynamic viscosity of water given by Guvanasen and Chan (2000), ρ_{l0} denotes the intrinsic liquid density at reference temperature T_0, ∇ denotes the space gradient, and β_l is defined in Eq. (6). Clearly, the dynamic viscosity and the density of the liquid phase are functions of temperature, and the hydraulic permeability is a function of both temperature and void ratio.

The classic continuity equation for the liquid and the solid phase is expressed as

$$\frac{\partial(\rho_l\phi_l)}{\partial t} + \nabla\cdot(\rho_l\phi_l\{v_l\}) = 0 \tag{11a}$$

$$\frac{\partial\left[\rho_s(1-\phi_l)\right]}{\partial t} + \nabla\cdot\left[\rho_s(1-\phi_l)\{v_s\}\right] = 0 \tag{11b}$$

where $\rho_s = \rho_{s0}[1-\beta_s(T-T_0)]$ and ρ_{s0} is the intrinsic solid density at reference temperature T_0. Note that

$$\nabla\cdot\{v_s\} = -\dot{\varepsilon}_v \text{ and } \rho_d = \rho_s(1-\phi_l) \tag{12}$$

Combining Eqs. (10)-(12) gives

$$-A_1\dot{\varepsilon}_v - A_2\dot{T} + A_1\nabla\cdot\{v\} - \beta_l\{v\}^T\nabla T = 0$$
$$\text{with } A_1 = 1-\beta_l(T-T_0) \text{ and } A_2 = \beta_l\phi_l + \left[1-\beta_l(T-T_0)\right]\beta_s\rho_{s0}\frac{\rho_d}{\rho_s^2} \tag{13}$$

Define the prescribed seepage velocity vector or pore pressure on the hydraulic boundary S_p as $\{\tilde{v}\} = \{\tilde{v}_r, \tilde{v}_z\}$ and p_s. Then, the axisymmetric form of the hydraulic governing equation can be derived as

$$[H_\varepsilon]\{\dot{a}\} - [H]\{\dot{T}\} + [H_p]\{p\} + [H_T]\{T\} = \{F_p\} \tag{14}$$

where the matrices are defined in the Appendix. The first term on the left represents the rate of deformation of the soil skeleton, and the second to fourth terms express the rate of deformation of the liquid phase due to thermal expansion, forced convection, and free convection, respectively. The equation takes into consideration the coupled effect of

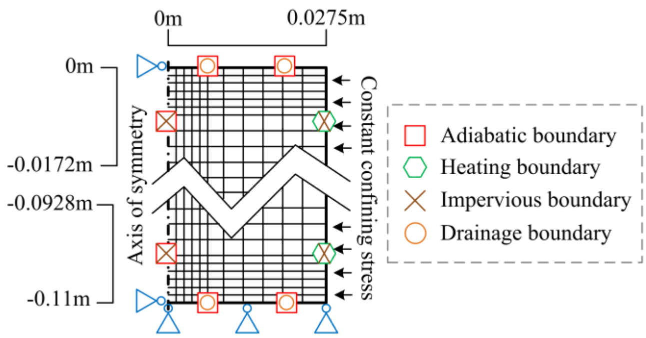

Fig. 1 FE mesh and axisymmetric boundary conditions for triaxial drained heating

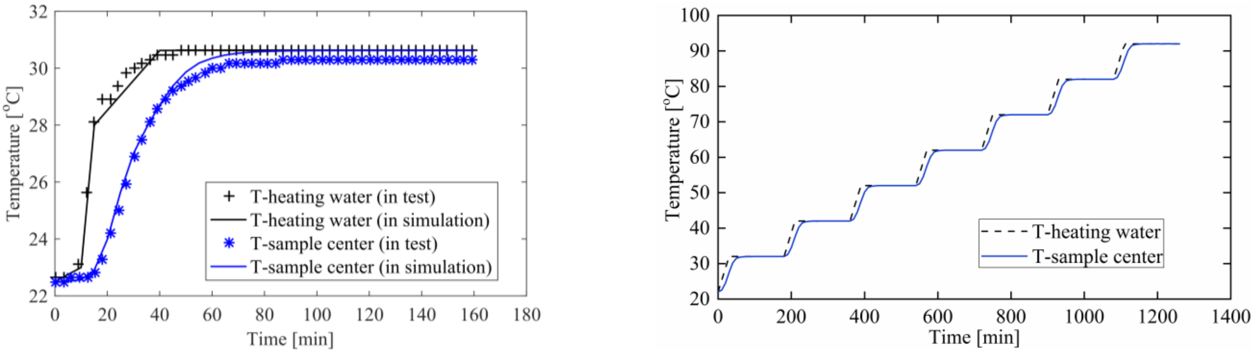

(a) Calibration of the thermal conductivity (b) The overall heating path

Fig. 2 Temperature evolution in the triaxial drained heating tests

deformable water and soil skeleton, temperature, and Darcy's law.

3.3 Thermal field formulation

The equation of transient heat transfer is formulated based on the law of energy conservation.

$$\left(\sum \rho_\alpha \phi_\alpha c_\alpha\right)\dot{T} - \lambda\left(\frac{1}{r}\frac{\partial}{\partial r}\left(r\frac{\partial T}{\partial r}\right) + \frac{\partial^2 T}{\partial z^2}\right) + \rho_l \phi_l c_l \{v\}^T \nabla T = 0 \quad (15)$$

where ρ_α, ϕ_α and c_α stand for the intrinsic density, the volume fraction, and the specific heat capacity, respectively, of the α phase (solid or liquid); λ is the averaged thermal conductivity of the saturated soils. The first term represents the increment of internal energy, the second term the heat transfer by conduction, and the third term the heat transfer by convection. The effect of radiation is not taken into consideration for simulations of laboratory-scale experiments, and the thermal conductivity is considered to be temperature independent.

Define the prescribed heat flux or temperature on the thermal boundary S_T as $\{\tilde{\eta}\}$ = $\{\tilde{\eta}_r, \tilde{\eta}_z\}$ and T_s. Then, the thermal governing equation can be derived as

$$[R]\{\dot{T}\} + [R_T]\{T\} = \{F_T\} \quad (16)$$

where the matrices are expressed in the Appendix.

3.4 The fully coupled THM formulation

Assembling Eqs. (9), (14), and (16), the incremental form of the fully coupled THM formulation reads as

$$\begin{bmatrix} [K] & -[K_p] & -[K_T] \\ [H_\varepsilon] & 0 & -[H] \\ 0 & 0 & [R] \end{bmatrix} \begin{Bmatrix} \{\dot{a}\} \\ \{\dot{p}\} \\ \{\dot{T}\} \end{Bmatrix} + \begin{bmatrix} 0 & 0 & 0 \\ 0 & [H_p] & [H_T] \\ 0 & 0 & [R_T] \end{bmatrix} \begin{Bmatrix} \{a\} \\ \{p\} \\ \{T\} \end{Bmatrix} = \begin{Bmatrix} \{F\} \\ \{F_p\} \\ \{F_T\} \end{Bmatrix} \quad (17)$$

The mechanical and hydraulic governing equations are THM-coupled, whereas the thermal governing equation is TH-coupled. The effect of heat transfer and the influence of pore pressure on the thermal field is expressed in $[R_T]$. The code adopts the 8-noded isoparametric quadrilateral elements using 2 x 2 Gauss rules for the numerical integration. The constitutive state variables and the temperature dependent FE variables are renewed in each iteration. For each material, 18 parameters need to be assigned. The definitions and units of the parameters are illustrated in Table 1.

To validate the newly developed THM coupled formulation and the FE code, a series of single-field and multi-field benchmark analyses has been conducted, such as the bearing capacity of strip footing, the isothermal 1D consolidation of a soil column, and the 1D THM processes in saturated geomaterial (Suvorov and Selvadurai 2009). Detailed validation and verification of the FE code can be found in Wang (2018).

4. Numerical simulation of laboratory tests

In the following, two typical series of drained heating tests of saturated clays from the literature are simulated. It is shown that not only is the FE implementation able to reproduce the experimental curves, but it can also provide insights into the physical mechanisms of thermally induced volume change.

4.1 Triaxial drained heating tests on Kaolin clay

Cekerevac and Laloui (2004) carried out a series of triaxial drained heating tests on Kaolin clay. The soil samples are 0.055 m in diameter and 0.11 m in height. Heating was obtained by placing the heater around the sample. Drainage was allowed on the top and bottom of the sample. The samples were first isotropically consolidated to 600 kPa at room temperature (22°C), then unloaded to 400 kPa, 300 kPa, 100 kPa, and 50 kPa to obtain OCR values of 1.5, 2, 6, and 12, respectively. Finally, under constant confining stresses, the samples were heated from 22°C to 90°C at a rate of 10°C per 3 h. The FE mesh and the axisymmetric boundary conditions for the triaxial drained heating are depicted in Fig. 1.

To simulate the test results, the parameters in the FE analyses relating to the thermal field are first calibrated. In the present case, the effect of heat convection is insignificant compared with that of heat transfer. Then, according to the theory of heat transfer, the transfer of heat is eventually determined by the thermal diffusivity expressed as $\alpha=\lambda/(\rho c)$, where λ is the thermal conductivity, ρ is the saturated soil density, and c is the averaged specific heat of the system. The specific heats of Kaolin and water are set as 1400 and 4200 J/kg/°C, respectively, and the initial saturated density of the samples is 1820 kg/m^3 (Cekerevac and Laloui 2004). Therefore, the only parameter needed for calibration is the thermal conductivity of the system.

Fig. 2(a) presents the results of a calibration test by Cekerevac and Laloui (2004) for the normally consolidated clay. It is shown that the time lag between the start of heating (temperature begins to change on the heating boundary) and the equilibration of temperature at the center is about 60 min for a heating step of about 8°C. This clearly indicates the uneven temperature distribution within the sample. By setting the thermal conductivity as λ=0.833 W/m/K, the FE analysis provides a satisfactory match of the temperature evolution at the center. Simulation of the whole heating path, including seven steps, according to the test description, is shown in Fig. 2(b).

The values of κ_0 and b_k, which relate to the hydraulic permeability, are listed in Table 2. According to Eq. (10), the selected values give the sample an initial permeability of 3 × 10^{-9} m/min, which has been validated by Zhang and Kurimoto (2016) and is reasonable for the saturated Kaolin clay.

Finally, the constitutive parameters of the extended GSH model for Kaolin clay are adopted from Zhang and Cheng (2016), who presented a detailed calibration process and satisfactory simulations on the constitutive level. The values of the parameters are listed in Table 2.

The major simulation results are discussed below.

4.1.1 Excess pore pressure generation

As mentioned in section 1, complete drainage is sometimes not achieved for the triaxial heating tests with drainage boundaries due to the low permeability of the clay sample and the high heating rate. If thermally induced excess pore pressure is generated at the center of the sample, the pore pressure will induce primary consolidation and affect the ultimate volume change. Therefore, the first task of the present simulation is to investigate the generation and distribution of the thermally induced excess pore pressure.

Table 2 Parameters used for the drained heating test simulations

Category	Parameter	Kaolin clay	Soft Bangkok clay
Isothermal hyperelasticity	B_0	2.35×10^6	6.25×10^6
	B_1	4.38×10^{-3}	4.80×10^{-3}
	c	2.38×10^{-2}	0.01
	ξ	4.44×10^{-2}	0.24
Isothermal plasticity	m_1	3.33×10^{-1}	1.25
	m_2	435.60	126.25
	m_3	0.40	0.1
	m_4	110	200
Thermoelastic coupling	β_s	1.80×10^{-5}	1.00×10^{-5}
	ϕ_{b0}	0.40	0.20
	ρ_{s0}	2624	1430
Thermoplastic coupling	α_{bf}	3.57×10^{-2}	0.04
	k_g	7.20×10^{-2}	0.02
	m_6	5.00×10^{-9}	3.00×10^{-8}
Intrinsic permeability	κ_0	3.20×10^{-21}	4.00×10^{-20}
	b_k	3.80	2.10
Energy conservation equation	c_s	1400	1400
	λ	0.83	1.50

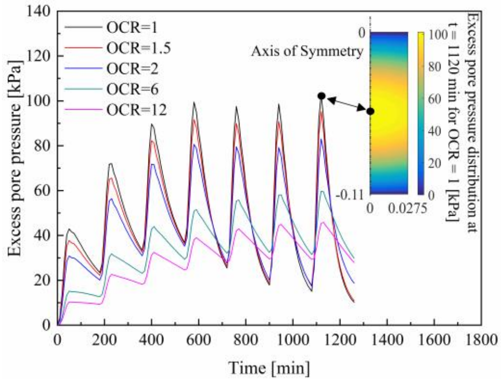

Fig. 3 Pore pressure evolution at the center of samples of different OCR values

Based on the test procedures described above and the chosen parameters, the pore pressure evolution at the center of the samples during heating is shown in Fig. 3. It is found that noticeable excess pore pressure is generated at the center of the sample, and the magnitude of the excess pore pressure varies with the OCR value. For OCR = 1, the maximum pore pressure at the center is about 17% of the isotropic confining stress, and the residual pore pressure at the end of heating is about 1.7% of the isotropic confining stress. The magnitude of the residual pore pressure is

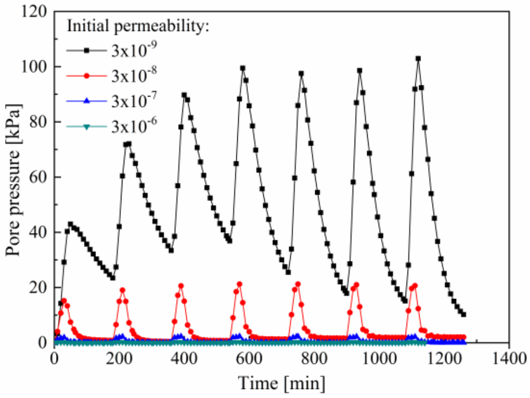

Fig. 4 Effect of initial permeability on the pore pressure evolution at the center for OCR = 1

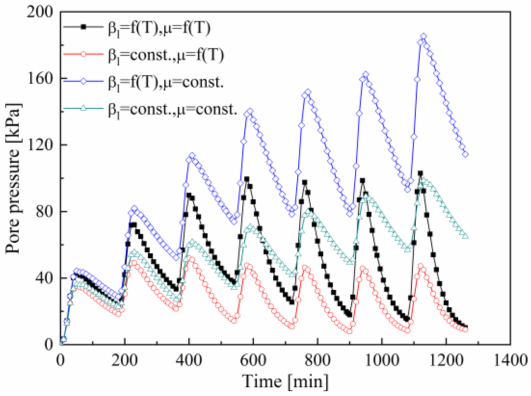

Fig. 5 Effect of the temperature dependence of the dynamic viscosity and the thermal expansion coefficient of water on the pore pressure evolution at the center for OCR = 1

similar to the observations by Vega and McCartney (2015) in the drained heating test of the normally consolidated Bonny clay.

During each of the seven heating steps, excess pore pressure first accumulates because of heating. Then, excess pore pressure dissipates as the temperature on the heating boundary maintains constant. The speed of excess pore pressure dissipation decreases with increasing OCR values, mainly because the seepage velocity is a function of the magnitude of excess pore pressure. Fig. 3 also shows the uneven distribution of excess pore pressure within the normally consolidated sample when the heating boundary first reaches the peak temperature. It is clear that the excess pore pressure at the top and bottom ends remains zero because of the drainage boundaries, whereas the maximum excess pore pressure appears at the center of the sample.

The existence of excess pore pressure brings about two important mechanisms for the volumetric change of clays. Firstly, the thermally induced primary consolidation adds to the irreversible contractive volumetric strain. Secondly, as shown in Fig. 3, when the temperature reaches 90°C, there remains noticeable accumulated pore pressure at the center. This gives rise to a reduction of the effective stress and, accordingly, a decrease of elastic volumetric strain (compression as positive). Thus, the two mechanisms have opposite effects on the volume change. The first mechanism is more significant for the normally consolidated sample, whereas the second mechanism is of more importance for the heavily overconsolidated sample because its residual pore pressure relative to the confining pressure is much higher. If the temperature maintains at 90°C, the residual excess pore pressure will gradually be dissipated, and the effective stress will eventually recover. However, under repeated thermal cycles, the excess pore pressure may not be dissipated and may result in a significant reduction of the effective stress. This phenomenon has a negative impact on the long-term stability of energy foundations. The quantitative contribution of the excess pore pressure to the volume change is discussed in the next section.

In fact, the magnitude of the excess pore pressure generated is closely related to the chosen hydraulic parameters. If the initial permeability is increased from 3×10^{-9} m/min to 3×10^{-8} m/min, 3×10^{-7} m/min, and 3×10^{-6} m/min, which means that the parameter κ_0 changes from 3.2×10^{-21} m^2 to 3.2×10^{-20} m^2, 3.2×10^{-19} m^2, and 3.2×10^{-18} m^2, respectively, the pore pressure evolution at the center for the case of OCR = 1 is depicted in Fig. 4. It is shown that by increasing the initial permeability by one order of magnitude, the pore pressure is able to dissipate completely within each of the seven heating steps. Therefore, the hydraulic permeability needs to be carefully decided in order to obtain an accurate simulation of the excess pore pressure.

Another factor worth mentioning is the temperature dependence of the dynamic viscosity and the thermal expansion coefficient of pore fluids. Previous THM-coupled analyses sometimes treated the two physical quantities as constants (e.g., Di Donna and Laloui 2015b, Zhang and Kurimoto 2016). According to Eq. (6) and Eq. (10), from 22°C to 90°C, the thermal expansion coefficient of water is going to triple its value, whereas the dynamic viscosity of water will drop to one-third of its initial value. An increase of the thermal expansion coefficient of water is expected to increase the generation of pore pressure during heating, because it adds to the compression between the solid phase and the liquid phase. In the meantime, a decrease of the dynamic viscosity of water leads to an increase of seepage velocity at elevated temperature, which may decrease the magnitude of pore pressure. Taking the heating tests of normally consolidated samples as an example, Fig. 5 presents the importance of considering the temperature dependence of the two physical quantities. If the thermal expansion coefficient of water is set as a constant (using the value at initial temperature, refer to the red curve), although the final pore pressure at the center may not deviate from the original analysis (refer to the black curve), the pore pressure evolution during heating and the volumetric contraction due to primary consolidation may be underestimated. In contrast, if the dynamic viscosity of water is set as a constant (using the value at the initial temperature, refer to the blue curve), the pore pressure accumulation may be significantly overestimated. Setting both physical quantities as constants (see the green curve) may more or less counterbalance the error of the above two cases, but it may as well wrongly predict the pore pressure

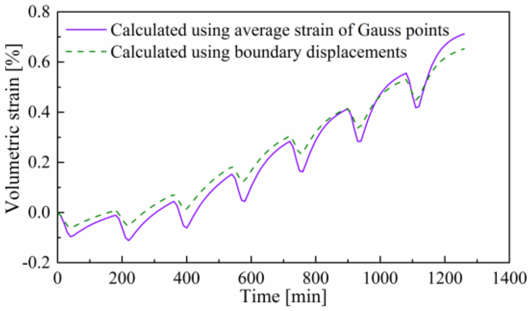

Fig. 6 Two ways of indicating the volumetric strain for the FE analyses

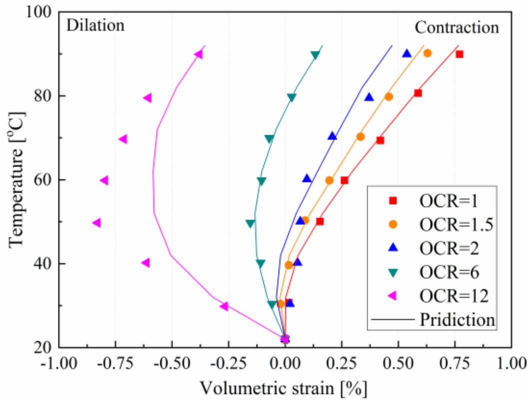

Fig. 7 Comparison between measured and predicted thermally induced volumetric strain for Kaolin

evolution and the final magnitude. Therefore, in the analyses hereinafter, the two physical quantities are always considered to be temperature dependent.

4.1.2 Evolution of volumetric strain

Two methods can be used to derive the overall volumetric strain of the clay samples in FE analyses, as shown in Fig. 6 for the case of OCR = 1. The first method is to calculate the averaged volumetric strain of each Gauss point. The second is to find out the boundary displacement of the sample and then compare it to the total volume. The choice in fact depends on how the volumetric strain was measured experimentally. In the triaxial tests by Cekerevac and Laloui (2004), the volumetric strain was calculated from the volume of water expelled from the sample. In this sense, the first method should be used because the volume of expelled water to some extent reflects the average of uneven deformation within the sample. In section 4.2, it is shown that a dial gage was used for the strain measurement of the oedometer tests by Abuel-Naga *et al.* (2006). Because only the displacement of the top boundary was measured, the second method may be better for this case. Although the calculation results of the two methods are not significantly different, as shown in Fig. 6, the current paper uses both methods accordingly for revealing the real measurement modes and for precision.

As can be seen in Fig. 6, the volumetric strain may decrease and increase during each of the seven heating steps because of the generation and dissipation of excess pore pressure. In the following figures, to be in accordance with the measured data, only the volumetric strains at the last minute of each heating step are selected to form the evolution curve of the thermally induced volumetric strain.

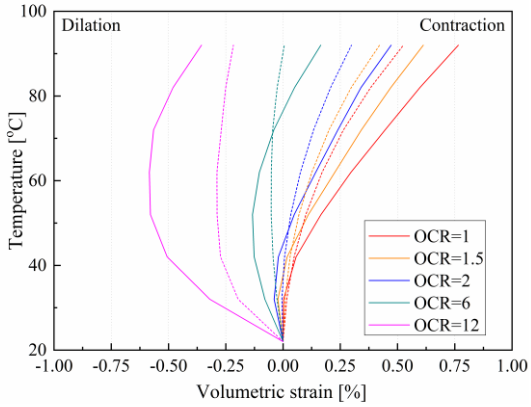

Fig. 8 Comparison of the predicted results using THM-coupled analyses and TM-coupled analyses (the solid lines are THM predictions, and the corresponding dashed lines are TM predictions)

Fig. 7 illustrates the comparison between measured and predicted thermally induced volumetric strains for Kaolin clay of different OCR values. The FE analyses provide satisfactory agreement with the observations by Cekerevac and Laloui (2004). The volumetric contraction is most obvious for the case of OCR = 1, with a maximum volumetric strain of 0.75% at 90 °C, whereas for the case of OCR = 12, a large dilation is observed and simulated. The results indicate that the material shows a thermoelastic-thermoplastic response when subjected to normally consolidated or lightly overconsolidated conditions and a thermoelastic response when subjected to heavily overconsolidated conditions. It should be noted the thermal contraction of clays is of major concern in the design and settlement prediction of energy foundations.

According to the simulation results, four physical mechanisms are considered to be responsible for the observed behaviors. The first mechanism is the principle of thermal expansion, which states that a material expands during heating and contracts during cooling according to its coefficient of thermal expansion. This elastic behavior is explicitly expressed in Eq. (1). It should be mentioned that the consideration of the thermal expansion coefficient of the adsorbed water is important for this mechanism. Without the contribution of the adsorbed water to the thermal expansion coefficient of the soil skeleton, the elastic dilation of the samples, especially for the case of OCR = 12, cannot be accurately predicted. The second is the constitutive thermoplastic mechanism, also known as thermal creep. According to the extended GSH model, an elevated temperature leads to the mass exchange from adsorbed water to free water (Eq. (4)), which causes the increase of irrecoverable volumetric strain defined in Eq. (3). The above two mechanisms are the main thermo-mechanical mechanisms if the phenomena are to be simulated on the constitutive level (e.g., Abuel-Naga *et al.* 2007, Cui *et al.* 2000, Di Donna and Laloui 2015a, Hueckel and Borsetto 1990, Laloui and François 2009, Zhang and

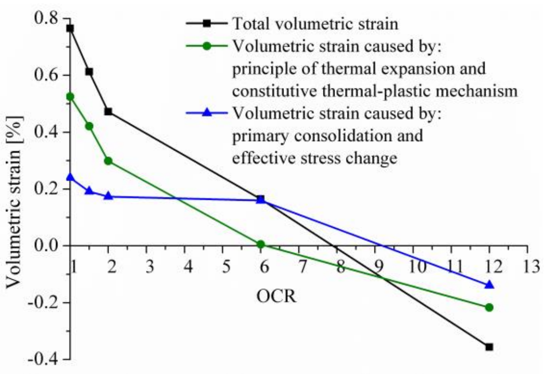

Fig. 9 Quantitative contribution of the physical mechanisms to the thermally induced volumetric strain in relation to OCR

Cheng 2016, Zymnis *et al.* 2018a), although the specific expressions and explanations of the thermoplasticity may vary according to different models.

The next two mechanisms are the thermally induced primary consolidation and the reduction of effective stress, which were introduced in section 4.1.1. Both mechanisms relate to the generation of excess pore pressure, thus do not exist in the constitutive-level simulation of tests with drainage boundaries. The mechanisms were not discussed by previous literature for the heating tests and are therefore the new findings of the present study. The thermally induced primary consolidation and the constitutive thermoplastic mechanism together form the irreversible volumetric contraction, whereas the reduction of effective stress and the principle of thermal expansion together contribute to the elastic volumetric expansion.

Fig. 8 further shows the importance of the consideration of excess pore pressure at the given parametric conditions. In the figure, the solid curves indicate the predictions by the THM-coupled analyses, which is the same as in Fig. 7, whereas the dash curves are the predictions by TM-coupled analyses using the same set of parameters. The TM-coupled analyses cannot consider the excess pore pressure and are thereby assumed in complete drainage conditions. For the cases of OCR = 1, 1.5, and 2, as compared to the TM predictions, the THM predictions show a slight dilation at the initial two heating stages, then a major contraction at subsequent heating stages. The slight dilation happens because at early stages, the generation of positive excess pore pressure and its influence on the elastic strain reduction is more effective than the primary consolidation. In later stages, however, the primary consolidation and its resulting plastic strain become more obvious, thus contributing to the major contraction. For the cases of OCR = 6 and 12, the thermal expansion in the THM predictions is more significant than in the TM predictions, due to the reduction of effective stress as a result of the pore pressure accumulation. In fact, the maximum volumetric expansion of 0.6% at 60°C for the case of OCR = 12 is not theoretically possible if only the principle of thermal expansion is considered. This highlights the contribution of excess pore pressure accumulation to the volume change of clay during heating.

Fig. 9 illustrates the quantitative contribution of the four mechanisms to the thermally induced volumetric strain in relation to OCR in the THM predictions at the assumed parametric conditions. For the cases of OCR = 1 and OCR = 12, the two mechanisms relating to excess pore pressure contribute to about 30% and 40% of the volumetric contraction or dilation, respectively. It is interesting to find that for OCR = 6, the effect of the principle of thermal expansion and that of the constitutive thermoplastic mechanism are counterbalanced. Consequently, the total volumetric contraction is in fact governed by the primary consolidation.

It is also worth mentioning that the uneven temperature distribution can affect the volumetric strain induced by the constitutive thermoplastic mechanism. By comparing the results of TM-coupled analyses using the normal thermal conductivity or an infinite thermal conductivity (for homogeneous temperature distribution), it is found that the latter case may significantly overestimate the plastic volumetric strain accumulation. For OCR = 1, assuming a homogeneous temperature distribution may overestimate 68% of the thermal contraction, whereas for OCR = 12, it may underestimate 57% of the thermal volumetric expansion. Therefore, the consideration of transient heat transfer is important for an accurate prediction of the triaxial drained heating test.

4.2 One-dimensional drained heating tests on soft Bangkok clay

To investigate the thermal behavior of soft Bangkok clay, Abuel-Naga *et al.* (2006) conducted a series of drained heating tests using a conventional oedometer with a ring heater around the sample cell. Drainage was allowed on both ends of the oedometer. The clay samples, 75 mm in diameter and 20 mm in height, were first consolidated under an axial stress of 200 kPa. Three samples were then unloaded to obtain OCR values of 2, 4, and 8. Finally, the samples were subjected to a heating-cooling cycle of 22-90-22°C. The incremental heating stage took about 24400 min (17 days).

The calibration test by Abuel-Naga *et al.* (2006) showed that the time to attain the required temperature increase at the center of the sample was around 25 min for a heating step of 68°C. Using the same approach as described in section 4.1, the thermal conductivity is calibrated as $\lambda = 1.5$ W/m/K. By setting $\kappa_0 = 4 \times 10^{-20}$ m^2 and $b_k = 2.1$, the hydraulic permeability according to Eq. (10) is in agreement with the measurement by Abuel-Naga *et al.* (2006) using the constant head permeability test, as shown in Fig. 10.

The constitutive model parameters of the soft Bangkok clay are calibrated based on the method proposed by Zymnis *et al.* (2015). The isothermal hyperelastic parameters (B, B_1, c, x) and the plastic parameters (m_1, m_2, m_3, m_4) are calibrated from the 1D compression tests (Abuel-Naga *et al.* 2007a). The thermoelastic parameters (b_s, r_{s0}) are given by Abuel-Naga *et al.* (2006). The initial volume fraction of adsorbed water (f_{b0}) is estimated from the laboratory measurements by Zymnis *et al.* (2018b). The thermoplastic parameters (a_{bf}, k_g, m_6) are calibrated from the

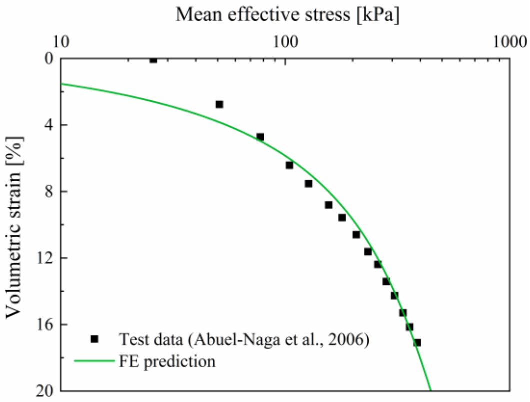

Fig. 11 Simulation of the isotropic consolidation behavior of soft Bangkok clay at room temperature

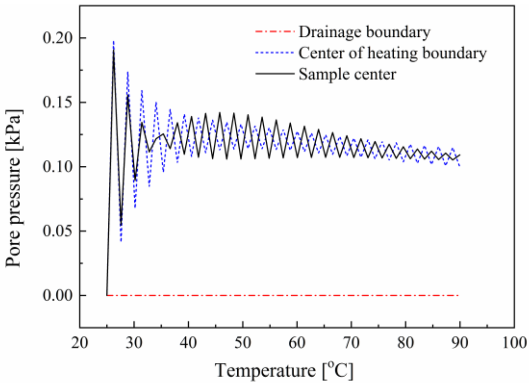

Fig. 12 Pore pressure evolution in the 1D drained heating test of normally consolidated soft Bangkok clay

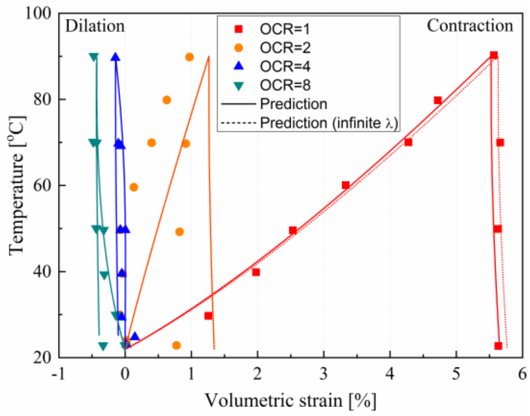

Fig. 13 Comparison between the test data and the FE predictions of the volumetric strain of soft Bangkok clay under 1D drained heating-cooling cycle

1D drained heating test of the normally consolidated sample (Abuel-Naga *et al.* 2006). It should be mentioned that Zymnis *et al.* (2015) also calibrated the parameters of the extended GSH model for the soft Bangkok clay using the same procedures. Meanwhile, the formulations in the present paper is somewhat different from Zymnis *et al.* (2015), resulting in the difference in the parameter values. Fig. 11 presents the isotropic compression curve at room temperature for the soft Bangkok clay. Note that the isotropic stress path is different from the 1D stress path used for calibration. Therefore, Fig. 11 serves as a blind prediction. The agreement between the FE simulation and the experimental results validates the accuracy of the model and the calibrated isothermal parameters listed in Table 2.

According to the test conditions mentioned above, the pore pressure evolution during the heating stage in the FE analysis for the case of OCR = 1 is illustrated in Fig. 12. Compared to the triaxial tests described in section 4.1, the 1D heating tests possess a shorter drainage path (10 mm compared to 55 mm), a much longer heating period (17 days compared to 1 day), and a permeability of the same order of magnitude. Therefore, the excess pore pressure generated herein is very small (0.1% of confining stress), and its influence on the volumetric behavior is negligible. In other words, the THM-coupled simulation and the TM-coupled simulation of the current case should provide similar results.

Fig. 13 shows the comparison between the test data and FE simulations of the volumetric strain of soft Bangkok clay under a drained heating-cooling cycle. The case of OCR = 1 has been used for the calibration of the thermoplastic parameters and is therefore a back-prediction, whereas the rest are blind simulations. In general, a satisfactory reproduction of the test data is obtained. The solid lines represent the normal THM prediction, whereas the dashed lines represent the THM prediction using an infinite thermal conductivity (simulating homogeneous temperature distribution). For the cases of OCR = 2, 4, and 8, the two sets of lines overlap each other, whereas for OCR = 1, there is only a slight difference. This phenomenon indicates that the effect of uneven temperature distribution in the current test condition is insignificant, mainly because the time required to reach temperature equilibrium (25 min) is very short as compared to the total heating period. In this sense, the FE analyses and constitutive-level simulations of the current tests may provide very close results.

Comparing Fig. 13 with Fig. 7, it is shown that the thermal contraction of the normally consolidated soft Bangkok clay is nearly seven times that of Kaolin clay. The reason for the phenomenon may relate to the interaction between clay particles and the adsorbed water. According to the DLVO theory (Derjaguin *et al.* 1987) and meso-scale experimental results (García-García *et al.* 2006, Li *et al.* 2007), the disjoining pressure (or swelling pressure) of adsorbed water may increase with temperature. Several researchers (e.g., Mitchell 1993, Plum and Esrig 1969) proposed that the increase of disjoining pressure would lead to the plastic redistribution of the saturated soil mass. Furthermore, it is commonly accepted that the disjoining pressure of smectite is much larger than that of kaolinite. Because soft Bangkok clay consists of 54-71% smectite and 28-36% kaolinite, it is reasonable that a certain elevated temperature may give rise to more intensive plastic redistribution of soft Bangkok clay than of Kaolin clay. In the extended GSH model, the mechanism related to the adsorbed water is quantitatively expressed in Eq. (4) by assuming a larger m_6 for the soft Bangkok clay.

5. Conclusions

Based on the extended GSH model, a novel axisymmetric finite element (FE) program is developed for analyzing the thermo-hydro-mechanical (THM) coupled behaviors of saturated clays. The aim of this paper is to investigate the physical mechanisms for the thermally induced volume change of clays. For this purpose, the proposed FE program is applied for the simulation of two existing series of experiments, the triaxial drained heating tests on Kaolin clay, and the 1D drained heating tests on soft Bangkok clay. The following are the major findings:

- In general, the FE predictions are in satisfactory agreement with the experimental data for the thermally induced volumetric strains of different OCR values. For the triaxial drained heating tests, different from the assumptions made in the constitutive-level simulations by previous researchers, the analyses indicate that noticeable inhomogeneous pore pressure may be generated within the samples due to the low permeability and the high heating rate. The temperature dependence of the thermal expansion coefficient and the dynamic viscosity of water is essential for the accurate prediction of the excess pore pressure evolution. For the 1D drained heating tests, the excess pore pressure generation is negligible because of the shorter drainage path and the lower heating rate.
- Four physical mechanisms govern the development of the volumetric strains: a) the principle of thermal expansion, b) the constitutive thermoplastic relation (also known as thermal creep), c) the thermally induced primary consolidation due to excess pore pressure dissipation, and d) the decrease of effective stress due to accumulated excess pore pressure. The first two mechanisms can be properly accounted for in both constitutive level and FE level simulations, whereas the second two mechanisms can only be taken into consideration on the FE level. Under the assumed material parametric conditions, it is found that the latter two mechanisms can contribute to about 30% of the volumetric contraction for the case of OCR = 1 and nearly 40% of the volumetric expansion for OCR = 12. Although derived from simulations of laboratory experiments, the four physical mechanisms are also applicable for the explanation of the temperature-triggered ground settlement at field scale.
- The thermal volumetric behaviors of clays are of major concern for geo-energy engineering applications. With future works such as the implementation of structural elements and soil-structure interfaces, the proposed FE program is expected to provide a new approach for the design and calculation of applications such as energy piles and energy tunnels in soft soils.

Acknowledgments

This work was supported by National Science Foundation of China (NSFC, grant number: 51778338) and the 7th Framework Program for Research of European Commission (grant number: 612665).

References

Au, F.T.K. and Du, J.S. (2004), “Prediction of ultimate stress in un-bonded prestressed tendons”, *Mag. Concrete Res.*, **56**(1), 1-11. https://doi.org/10.1680/macr.2004.56.1.1.

Abuel-Naga, H.M., Bergado, D.T. and Bouazza, A. (2007a), “Thermally induced volume change and excess pore water pressure of soft Bangkok clay”, *Eng. Geol.*, **89**(1-2), 144-154. https://doi.org/10.1016/j.enggeo.2006.10.002.

Abuel-Naga, H.M., Bergado, D.T., Bouazza, A. and Ramana, G.V. (2007b), “Volume change behaviour of saturated clays under drained heating conditions: Experimental results and constitutive modeling”, *Can. Geotech. J.*, **44**(8), 942-956. https://doi.org/10.1139/t07-031.

Abuel-Naga, H.M., Bergado, D.T., Ramana, G.V., Grino, L., Rujivipat, P. and Thet, Y. (2006), “Experimental evaluation of engineering behavior of soft Bangkok clay under elevated temperature”, *J. Geotech. Geoenviron. Eng.*, **132**(7), 902-910. https://doi.org/10.1061/(ASCE)1090-0241(2006)132:7(902).

Bai, B. and Shi, X. (2017), “Experimental study on the consolidation of saturated silty clay subjected to cyclic thermal loading”, *Geomech. Eng.*, **12**(4), 707-721. http://doi.org/10.12989/gae.2017.12.4.707.

Baldi, G., Hueckel, T. and Pellegrini, R. (1988), “Thermal volume changes of the mineral-water system in low-porosity clay soils”, *Can. Geotech. J.*, **25**(4), 807-825. https://doi.org/10.1139/t88-089.

Brandl, H. (2006), “Energy foundations and other thermo-active ground structures”, *Géotechnique*, **56**(2), 81-122. https://doi.org/10.1680/geot.2006.56.2.81.

Cekerevac, C. and Laloui, L. (2004), “Experimental study of thermal effects on the mechanical behaviour of a clay”, *Int. J. Numer. Anal. Meth. Geomech.*, **28**(3), 209-228. https://doi.org/10.1002/nag.332.

Cui, W., Tsiampousi, A., Potts, D.M., Gawecka, K.A. and Zdravković, L. (2020), “Numerical modeling of time-dependent thermally induced excess pore fluid pressures in a saturated soil”, *J. Geotech. Geoenviron. Eng.*, **146**(4), 04020007. https://doi.org/10.1061/(ASCE)GT.1943-5606.0002218.

Cui, Y.J., Sultan, N. and Delage, P. (2000), “A thermomechanical model for clays”, *Can. Geotech. J.*, **37**(3), 607-620. https://doi.org/10.1139/t99-111.

Derjaguin, B.V., Churaev, N.V. and Muller, V.M. (1987), *Surface Forces*, Plenum Publishing Corporation, New York, U.S.A.

Di Donna, A. and Laloui, L. (2015a), “Response of soil subjected to thermal cyclic loading: Experimental and constitutive study”, *Eng. Geol.*, **190**, 65-76. https://doi.org/10.1016/j.enggeo.2015.03.003.

Di Donna, A. and Laloui, L. (2015b), “Numerical analysis of the geotechnical behaviour of energy piles”, *Int. J. Numer. Anal. Meth. Geomech.*, **39**(8), 861-888. https://doi.org/10.1002/nag.2341.

García-García, S., Jonsson, M. and Wold, S. (2006), “Temperature effect on the stability of bentonite colloids in water”, *J. Colloid Interf. Sci.*, **298**(2), 694-705. https://doi.org/10.1016/j.jcis.2006.01.018.

Guvanasen, V. and Chan, T. (2000), “A three-dimensional numerical model for thermohydromechanical deformation with hysteresis in a fractured rock mass”, *Int. J. Rock Mech. Min. Sci.*, **37**(1-2), 89-106. https://doi.org/10.1016/S1365-1609(99)00095-7.

Hiebl, M. and Maksymiw, R. (1991), “Anomalous temperature dependence of the thermal expansion of proteins”, *Biopolymers*, **31**(2), 161-167. https://doi.org/10.1002/bip.360310204.

Hueckel, T. and Borsetto, M. (1990), “Thermoplasticity of saturaed clays: Experimentals constitutive study”, *J. Geotech. Eng.*, **116**(12), 1778-1796. https://doi.org/10.1061/(ASCE)0733-9410(1990)116:12(1778).

Hueckel, T. and Pellegrini, R. (1992), “Effective stress and water-pressure in saturated clays during heating-cooling cycles”, *Can.*

Geotech. *J*., **29**(6), 1095-1102. https://doi.org/10.1139/t92-126.

Jiang, Y. and Liu, M. (2007), "From elasticity to hypoplasticity: Dynamics of granular solids", *Phys*. *Rev*. *Lett*., **99**(10), 105501. https://doi.org/10.1103/PhysRevLett.99.105501.

Jiang, Y. and Liu, M. (2009), "Granular solid hydrodynamics", *Granul*. *Matter*, **11**(3), 139-156. https://doi.org/10.1007/s10035-009-0137-3.

Johnson, K.L. (1987), *Contact Mechanics*, Cambridge University Press, Cambridge, U.K.

Laloui, L. and François, B. (2009), "ACMEG-T: Soil thermoplasticity model", *J*. *Eng*. *Mech*., **135**(9), 932-944. https://doi.org/10.1061/(ASCE)EM.1943-7889.0000011.

Li, C., Kong, G., Liu, H. and Abuel-Naga, H. (2019), "Effect of temperature on behaviour of red clay-structure interface", *Can*. *Geotech*. *J*., **56**(1), 126-134. https://doi.org/10.1139/cgj-2017-0310.

Li, H., Long, J., Xu, Z. and Masliyah, J.H. (2007), "Flocculation of kaolinite clay suspensions using a temperature-sensitive polymer", *AIChE J*., **53**(2), 479-488. https://doi.org/10.1002/aic.11073.

Li, Y., Dijkstra, J. and Karstunen, M. (2018), "Thermomechanical creep in sensitive clays", *J*. *Geotech*. *Geoenviron*. *Eng*., **144**(11), 1-11. https://doi.org/10.1061/(ASCE)GT.1943-5606.0001965.

Mitchell, J.K. (1993), *Fundamentals of Soil Behavior*, John Wiley, New York, U.S.A.

Morinl, R. and Silva, A. (1984), "The effects of high pressure and high temperature on some physical properties of ocean sediments", *J*. *Geophys*. *Res*., **89**(3), 511-526. https://doi.org/10.1029/JB089iB01p00511.

Osipov, V.I.V. (2012), "Nanofilms of adsorbed water in clay: Mechanism of formation and properties", *Water Resour*., **39**(7), 709-721. https://doi.org/10.1134/S009780781207010X.

Plum, R.L. and Esrig, M.I. (1969), "Some temperature effects on soil compressibility and pore water pressures", *Proceedings of the 48th Annual Meeting of the Highway Research Board*.

Song, Z., Hao, Y. and Liu, H. (2020), "Analytical study of the thermo-osmosis effect in porothermoelastic responses of saturated porous media under axisymmetric thermal loadings", *Comput*. *Geotech*., **123**, 103576. https://doi.org/10.1016/j.compgeo.2020.103576.

Stewart, M.A. and McCartney, J.S. (2014), "Centrifuge modeling of soil-structure interaction in energy foundations", *J*. *Geotech*. *Geoenviron*. *Eng*., **140**(4), 04013044. https://doi.org/10.1061/(ASCE)GT.1943-5606.0001061.

Sultan, N., Delage, P. and Cui, Y.J. (2002), "Temperature effects on the volume change behaviour of Boom clay", *Eng*. *Geol*., **64**(2-3), 135-145. https://doi.org/10.1016/S0013-7952(01)00143-0.

Suvorov, A.P. and Selvadurai, A.P.S. (2009), "THM processes in a fluid-saturated poroelastic geomaterial: Comparison of analytical results and computational estimates", *Proceedings of the 3rd CANUS Rock Mechanics Symposium*, Toronto, Canada, May.

Tamizdoust, M.M. and Ghasemi-Fare, O. (2020), "A fully coupled thermo-poro-mechanical finite element analysis to predict the thermal pressurization and thermally induced pore fluid flow in soil media", *Comput*. *Geotech*., **117**, 103250. https://doi.org/10.1016/j.compgeo.2019.103250.

Towhata, I., Kuntiwattanaku, P., Seko, I. and Ohishi, K. (1993), "Volume change of clays induced by heating as observed in consolidation tests", *Soils Found*., **33**(4), 170-183. https://doi.org/10.3208/sandf1972.33.4_170.

Vega, A. and McCartney, J.S. (2015), "Cyclic heating effects on thermal volume change of silt", *Environ*. *Geotech*., **2**(5), 257-268. https://doi.org/10.1680/envgeo.13.00022.

Villar, M.V. and Lloret, A. (2004), "Influence of temperature on the hydro-mechanical behaviour of a compacted bentonite", *Appl. Clay Sci*., **26**(1-4), 337-350. https://doi.org/10.1016/j.clay.2003.12.026.

Wang, H. (2018), "Research on multi-scale and multi-field thermodynamic constitutive model and its finite element implementation for saturated geomaterials", Ph.D. Dissertation, Tsinghua University, Beijing, China.

Wang, H. and Cheng, X. (2017), "A thermodynamic model for rate-dependent geomaterials", *Proceedings of the Advances in Laboratory Testing and Modelling of Soils and Shales (ATMSS),* Villars-sur-Ollon, Switzerland, January.

Xu, S., Scherer, G.W., Mahadevan, T.S. and Garofalini, S.H. (2009), "Thermal expansion of confined water", *Langmuir*, **25**(9), 5076-5083. https://doi.org/10.1021/la804061p.

Zhang, F. and Kurimoto, Y. (2016), "How to model the contractive behavior of soil in a heating test", *Undergr*. *Sp*., **1**(1), 30-43. https://doi.org/10.1016/j.undsp.2016.05.001.

Zhang, Z.C. and Cheng, X.H. (2016), "A thermo-mechanical coupled constitutive model for clay based on extended granular solid hydrodynamics", *Comput*. *Geotech*., **80**, 373-382. https://doi.org/10.1016/j.compgeo.2016.05.010.

Zhang, Z. and Cheng, X. (2017), "A fully coupled THM model based on a non-equilibrium thermodynamic approach and its application", *Int*. *J*. *Numer*. *Anal*. *Meth*. *Geomech*., **41**(4), 527-554. https://doi.org/10.1002/nag.2569.

Zhou, C. and Ng, C.W.W. (2018), "A new thermo-mechanical model for structured soil", *Geotechnique*, **68**(12), 1109-1115. https://doi.org/10.1680/jgeot.17.T.031.

Zhu, Q.Y., Jin, Y.F., Shang, X.Y. and Chen, T. (2019), "A 1D model considering the combined effect of strain-rate and temperature for soft soil", *Geomech. Eng.*, **18**(2), 133-140. http://doi.org/10.12989/gae.2019.18.2.133.

Zymnis, D.M., Whittle, A.J. and Cheng, X. (2015), "TTS model for thermo-mechanical behavior of clay", *Proceedings of the XVI European Conference on Soil Mechanics and Geotechnical Engineering,* Edinburgh, Scotland, U.K., September.

Zymnis, D.M., Whittle, A.J. and Cheng, X. (2018a), "Simulation of long-term thermo-mechanical response of clay using an advanced constitutive model", *Acta Geotech*., **14**(2), 295-311. https://doi.org/10.1007/s11440-018-0726-6.

Zymnis, D.M., Whittle, A.J. and Germaine, J.T. (2018b), "Measurement of temperature-dependent bound water in clays", *Geotech*. *Test*. *J*., **42**(1), 232-244. https://doi.org/10.1520/GTJ20170012.

GC

Appendix

$$[D_\varepsilon]=\begin{bmatrix} \frac{\partial\sigma_r'}{\partial\varepsilon_r^e} & \frac{\partial\sigma_r'}{\partial\varepsilon_\theta^e} & \frac{\partial\sigma_r'}{\partial\varepsilon_z^e} & \frac{\partial\sigma_r'}{\partial\varepsilon_{rz}^e} \\ \frac{\partial\sigma_\theta'}{\partial\varepsilon_r^e} & \frac{\partial\sigma_\theta'}{\partial\varepsilon_\theta^e} & \frac{\partial\sigma_\theta'}{\partial\varepsilon_z^e} & \frac{\partial\sigma_\theta'}{\partial\varepsilon_{rz}^e} \\ \frac{\partial\sigma_z'}{\partial\varepsilon_r^e} & \frac{\partial\sigma_z'}{\partial\varepsilon_\theta^e} & \frac{\partial\sigma_z'}{\partial\varepsilon_z^e} & \frac{\partial\sigma_z'}{\partial\varepsilon_{rz}^e} \\ \frac{\partial\tau_{rz}'}{\partial\varepsilon_r^e} & \frac{\partial\tau_{rz}'}{\partial\varepsilon_\theta^e} & \frac{\partial\tau_{rz}'}{\partial\varepsilon_z^e} & \frac{\partial\tau_{rz}'}{\partial\varepsilon_{rz}^e} \end{bmatrix}$$

$$[D_T]=\begin{bmatrix} \frac{\partial\sigma_r'}{\partial T} & \frac{\partial\sigma_\theta'}{\partial T} & \frac{\partial\sigma_z'}{\partial T} & \frac{\partial\tau_{rz}'}{\partial T} \end{bmatrix}^T$$

$$[D_\rho]=\rho_d\begin{bmatrix} \frac{\partial\sigma_r'}{\partial\rho_d} & \frac{\partial\sigma_r'}{\partial\rho_d} & \frac{\partial\sigma_r'}{\partial\rho_d} & 0 \\ \frac{\partial\sigma_\theta'}{\partial\rho_d} & \frac{\partial\sigma_\theta'}{\partial\rho_d} & \frac{\partial\sigma_\theta'}{\partial\rho_d} & 0 \\ \frac{\partial\sigma_z'}{\partial\rho_d} & \frac{\partial\sigma_z'}{\partial\rho_d} & \frac{\partial\sigma_z'}{\partial\rho_d} & 0 \\ \frac{\partial\tau_{rz}'}{\partial\rho_d} & \frac{\partial\tau_{rz}'}{\partial\rho_d} & \frac{\partial\tau_{rz}'}{\partial\rho_d} & 0 \end{bmatrix}$$

$$\{\dot{Y}\}=\begin{bmatrix} (T_g)^{0.5}\varepsilon_r^e+(m_1-\frac{1}{3})(T_g)^{0.5}\varepsilon_v^e \\ (T_g)^{0.5}\varepsilon_\theta^e+(m_1-\frac{1}{3})(T_g)^{0.5}\varepsilon_v^e \\ (T_g)^{0.5}\varepsilon_z^e+(m_1-\frac{1}{3})(T_g)^{0.5}\varepsilon_v^e \\ (T_g)^{0.5}\gamma_{rz}^e \end{bmatrix}$$

$$[K]=\sum_{\Delta^e}\iint_{\Delta^e} B^T([D_\varepsilon]+[D_\rho])Brdrdz$$

$$[K_p]=\sum_{\Delta^e}\iint_{\Delta^e} B^T\{m\}N_p rdrdz$$

$$[K_T]=\sum_{\Delta^e}\iint_{\Delta^e} B^T[D_T]N_T rdrdz$$

$$\{F\}=\sum_{\Delta^e}\iint_{\Delta^e}\left(-B^T[D_\varepsilon]\{\dot{Y}\}+N^T\{\dot{g}\}[\rho_d+\rho_l(1-\frac{\rho_d}{\rho_s})]\right)rdrdz+\sum_{S_\sigma^e}\int_{S_\sigma^e}N^T\{\dot{s}\}rdS$$

$$[H_\varepsilon]=\sum_{\Delta^e}\iint_{\Delta^e}\left(A_1 N_p{}^T m^T B\right)rdrdz$$

$$[H]=\sum_{\Delta^e}\iint_{\Delta^e}\left(A_2 N_p{}^T N_T\right)rdrdz$$

$$[H_p]=\sum_{\Delta^e}\iint_{\Delta^e}\left(\frac{\kappa}{\mu}A_1(\nabla N_p)^T\nabla N_p\right)rdrdz$$

$$[H_T]=\sum_{\Delta^e}\iint_{\Delta^e}\left[\frac{\kappa}{\mu}\beta_l\left(N_p{}^T\{p\}^T(\nabla N_p)^T\nabla N_T-\rho_l N_p{}^T\{g\}^T\nabla N_T\right)\right]rdrdz$$

$$\{F_p\}=\sum_{S_p^e}\int_{S_p^e}\left[A_1 N_p{}^T\cdot(\tilde{v}_r+\tilde{v}_z)\right]rdS+\sum_{\Delta^e}\iint_{\Delta^e}\left[\frac{\kappa}{\mu}A_1\rho_l(\nabla N_p)^T\{g\}\right]rdrdz$$

$$[R]=\sum_{\Delta^e}\iint_{\Delta^e}\left(\sum\rho_\alpha\phi_\alpha c_\alpha\right)N_T{}^T N_T rdrdz$$

$$[R_T]=\sum_{\Delta^e}\iint_{\Delta^e}\left(\lambda(\nabla N_T)^T\nabla N_T+\rho_l\phi_l c_l\frac{\kappa}{\mu}\left[N_T{}^T\{p\}^T(\nabla N_p)^T\nabla N_T-\rho_l N_T{}^T\{g\}^T\nabla N_T\right]\right)rdrdz$$

$$\{F_T\}=-\sum_{S_T^e}\int_{S_T^e}\left[N_T{}^T\cdot(\tilde{\eta}_r+\tilde{\eta}_z)\right]rdS$$